PAPER

Check for updates

Photodegradation of antihistamine chlorpheniramine using a novel iron-incorporated carbon material and solar radiation†

A. F. Mar-Ortiz,[ab] J. J. Salazar-Rábago,*[a] M. Sánchez-Polo,[b] M. Rozalen, [iD] *[b] F. J. Cerino-Córdova[c] and M. Loredo-Cancino[a]

Water pollution due to emerging contaminants is a topic that should be researched to a greater extent because of the ignorance of adverse effects these pollutants may have on living beings. For this reason, the implementation of tertiary treatments is important for the removal of these contaminants from aqueous effluents including the heterogeneous photo-Fenton like (HPFL) process. In this investigation, an organic carbon xerogel incorporated with Fe^{3+} (XFe) has been used as a photocatalyst for the degradation of the antihistamine chlorpheniramine in an aqueous media with pH 3 at room temperature. The characterization of the material revealed the presence of Fe(III) and oxygenated groups on the surface as well as its ability to be activated with visible radiation, thereby, making it a viable material for the oxidation of contaminants present in the aqueous phase. The kinetic study has revealed that the degradation kinetic constants were 4.20×10^{-1} min^{-1} and 1.57×10^{-3} min^{-1} for HPFL and photolysis processes, respectively, revealing that the oxidation process is favored in the presence of the carbonaceous material. The by-products derived from various post-degradation processes presented low toxicity when verified by cytotoxicity tests. Moreover, the catalyst activation mechanism demonstrated that the process occurs through the formation of the ˙HO radical. In conclusion, the HPFL process was the most feasible for the degradation of chlorpheniramine in aqueous media, as it had greater interaction with the ˙HO radical in the rupture of the contaminant.

Water impact

The presence of antihistamines in the aquatic environment is an issue that must be addressed with particular relevance. Like many other contaminants, these drugs can affect living beings and directly impact their health. The implementation of advanced oxidation processes for their removal is being evaluated, considering its favorable results with different compounds.

Introduction

The problem of water pollution is increasingly alarming; according to estimations by the UN, 1500 km^3 of wastewater is generated annually, of which around 70% is released into freshwater sources without any previous treatment.[1] These water bodies can be polluted by the presence of various infectious agents, toxic chemicals or heavy metals; among these pollutants, emerging contaminants (EC) have attracted the attention of many researchers in the last decade. Particular importance should be paid to pharmaceutical compounds as canditates of this type of pollutants. Although, they are found in low concentrations, their presence is very frequent and complete knowledge of the possible effects they may have on living beings is lacking.[2]

Currently, the presence of these contaminants has been reported in various investigations; this is the case for various commonly used drugs, such as chlorpheniramine, diclofenac, and paracetamol.[3–5] Chlorpheniramine (CP) is a first-generation antihistamine that is mainly used to treat allergic symptoms and the common cold. The concentrations of CP detected in surface waters are between 3.34 and 9.53 ng L^{-1}.[6–8] Various investigations have reported several negative effects in marine biota as a consequence of the presence of different ECs in water.[7] In the case of CP, tests have only been carried out on *Dugesia japonica* to measure its acute survival.[9] Most wastewater discharges, especially those

[a] Universidad Autónoma de Nuevo León, Facultad de Ciencias Químicas, Av. Universidad s/n Cd. Universitaria, 66455 San Nicolás de los Garza, Nuevo León, Mexico. E-mail: jacob.salazarb@uanl.edu.mx
*[b] Department of Inorganic Chemistry, Faculty of Science, University of Granada, 18071 Granada, Spain. E-mail: marisarozalen@ugr.es; Tel: +34958242888*
[c] Universidad Autónoma de Nuevo León (UANL), Facultad de Ingeniería Mecánica y Eléctrica, 66455, San Nicolás de Los Garza, Nuevo León, Mexico
† Electronic supplementary information (ESI) available. See DOI: 10.1039/d0ew00413h

Paper

containing drugs, are due to urban waste,[10] pharmaceutical industries[4] and agro-industries;[11] wastewater from these sources is often directly discharged or arrives at wastewater treatment plants (WWTP), where the problem is only partially solved because the mainly used primary and secondary treatments are not effective enough to remove all the contaminants present. Consequently, the use of tertiary treatments for the complete removal of this type of contaminant has become interesting. Among these treatments, advanced oxidation processes (AOPs) stand out, where the use of oxidizing agents such as hydrogen peroxide, ozone, and chlorine promotes the degradation of various water pollutants through the generation of radical species such as $^{\bullet}HO$ and $O_2^{\bullet-}$. One method to produce these oxidant radicals is photocatalytic processes, which have already been used by other authors for the degradation of ECs;[12–14] the best known catalyst is homogeneous phase TiO_2, the main disadvantage of which is its activation in the ultraviolet region. In the same way, one of the most studied chemical processes presenting high removal rates of organic compounds in aqueous media is the Fenton-like process, which promotes the production of hydroxyl radicals ($^{\bullet}HO$) generated from the reaction of hydrogen peroxide (H_2O_2) and iron(III) salts. However, this entails the addition of salts to aqueous media,[15] which is contributing to the upsurge of interest in the immobilization of iron in various matrices[16–18] to favor the simple removal of this metal and the reduction of its leaching; in light of this, the previously mentioned process has been designated as "heterogeneous Fenton-like"[19] and can be seen in eqn (1)–(3). The three lines adjacent to Fe(III) symbolize that it is anchored to the material, where it is assumed that the Fe(III) shown in reaction 1 is regenerated by reaction 3; therefore, reaction 2 is the rate-limiting step.[20]

$$\equiv Fe^{III} + H_2O_2 = \equiv Fe^{III}H_2O_2 \tag{1}$$

$$\equiv Fe^{III}H_2O_2 \rightarrow \equiv Fe^{II} + HO_2 + H^+ \tag{2}$$

$$\equiv Fe^{II} + H_2O_2 \rightarrow \equiv Fe^{III} + {}^{\bullet}OH + OH^- \tag{3}$$
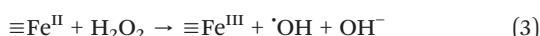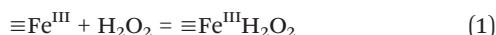
For this reason, the preparation of supports for catalysts is a viable alternative. Some of the carbonaceous materials that have gained importance in recent years are organic carbon xerogels, which present simple synthesis and whose textural and optical properties can be easily modified; thus, they are very interesting materials for incorporating diverse types of metal salts.[21] In addition to this, the implementation of a radiant energy source in the heterogeneous Fenton-like process is called the heterogeneous photo-Fenton like (HPFL) process, where the generation of $^{\bullet}HO$ radicals is even faster than in the previous process.

The specific objective of this investigation was to study the photodegradation of the drug chlorpheniramine through the use of Fe(III)-incorporated organic carbon xerogels, which were synthesized by a previously reported sol–gel method.[22]

The resulting materials were subjected to physicochemical and textural characterization; in addition, the degradation kinetics of CP was evaluated under different operating conditions, the possible mechanisms of activation of the material and drug degradation were determined, and finally, the cytotoxicity of the degradation by-products was evaluated.

Reagents

All chemical reagents used in the study were high-purity analytical grade and were supplied by Sigma-Aldrich, including formaldehyde (CH_2O), citric acid ($C_6H_8O_7$), sodium carbonate (Na_2CO_3), resorcinol ($C_6H_6O_2$), iron nitrate nonahydrate (Fe (NO_3)$_3$·9H$_2$O), and chlorpheniramine ($C_{16}H_{19}N_2Cl$). All solutions were prepared with ultrapure water obtained using a Milli-Q kit (18.3 MΩ cm). Fig. 1 shows the CP speciation diagram, which shows a basic molecule containing two basic groups: a pyridine nitrogen with pK_{a1} = 4.0 and a tertiary amine group with pK_{a2} = 9.2.[1] Table 1 shows some properties of chlorpheniramine.

Synthesis of xerogels

The synthesis of organic carbon xerogels (OCX) has been analyzed by various researchers;[23,24] in our case, we followed the methodology proposed by Orellana et al.,[22] with the variation of introducing citric acid as a ligand. The procedure for the reference material is briefly described below; without the presence of the metal (XBco), the ratios used were 0.15 R/F, 0.13 R/W and 100 R/C. Na_2CO_3 was the catalyst for XBco, while $Fe(NO_3)_3$ was used for the Fe-incorporated materials. According to the concentration of the Fe solution used in the synthesis, XFe-0.5, XFe-1.0 and XFe-1.5 designate concentrations of 0.5, 1.0 and 1.5 M, respectively.

Characterization of the materials

The morphological and textural characteristics of the resulting materials were obtained through scanning electron
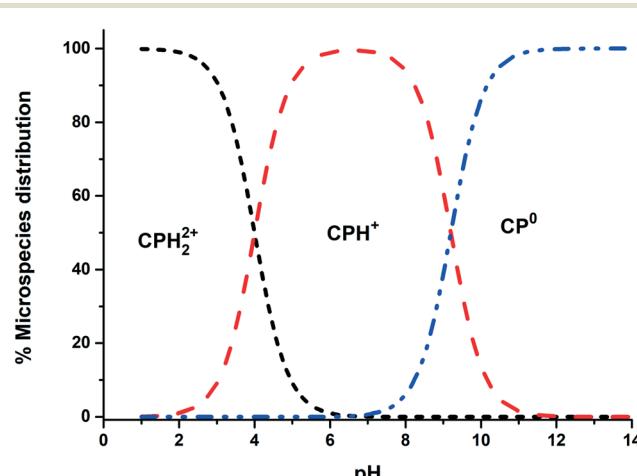
Fig. 1 Chlorpheniramine speciation diagram (1 mM).

Table 1 Molecular structure and properties of CP

Name and formula	Structure	MW (g mol^{-1})	Solubility (mg mL^{-1})	pK_a
Chlorpheniramine C$_{16}$H$_{19}$ClN$_2$		274.79	50	pK_{a1} = 4.0 pK_{a2} = 9.2

microscopy (SEM) (Philips, model XL30) and nitrogen physisorption (Micromeritics, model ASAP 2420). Furthermore, the surface physicochemical properties such as functional groups were evidenced by Fourier-transform infrared spectroscopy (FTIR) (JASCO, FT-IR-6300) and X-ray photoelectron spectroscopy (XPS) (Kratos, spectrometer Axis Ultra-DLD equipped with an Al Kα source). In addition, the band-gap energy and the optoelectronic properties of the materials were determined by UV-vis diffuse reflectance spectroscopy (CARY 4000 UV-vis spectrophotometer, equipped with an integrating sphere) and photoluminescence (PL) spectroscopy using a CARY VARIAN fluorescence spectrophotometer equipped with a Xe lamp as an excitation source to obtain PL spectra at a wavelength of 380 nm at room temperature (293 K).

Photodegradation experimental system

The drug photodegradation experiments were performed at pH 3 using an initial drug concentration of 15 mg L^{-1}, considering that many authors have used that concentration,[24,25] prepared from a 1000 mg L^{-1} standard solution. In the kinetics analysis, we measured the variation of the concentration as a function of time. The influence of some operational parameters, such as the type of irradiation (solar and UV), the dose of the catalyst (0.5.1 and 2 mg mL^{-1}) and the H$_2$O$_2$ concentration (50 100 and 150 μM), was also investigated. Moreover, two photoreactors were used; one had a mercury lamp (Heraeus Noble-Light TQ718-700W) attached in the center, which emits at 254 nm with a power of 15 W (795.8 W m^{-2}) and an energy consumption of 2865 kW h^{-1}; in the annular space of the photoreactor, there are 6 quartz tubes with 1 cm diameter and 35 mL capacity, which are constantly magnetically stirred individually and immersed in distilled water to maintain a constant temperature (25 °C) using a thermostat (Frigiterm). Meanwhile, the other photoreactor contained a xenon lamp in order to simulate solar radiation (SOLARBOX 1500, NEURTEK Instruments), which supplied radiant energy of 450 W m^{-2} and an energy consumption of 1620 kW h^{-1} and holds up to 3 quartz tubes of 35 mL arranged semi-horizontally with constant agitation and ventilation.

Analytical methods

Chromatographic system

The concentrations of chlorpheniramine (CP) in solution were determined by reversed phase high-performance liquid chromatography (HPLC) using a liquid chromatograph (Thermo-Fisher) equipped with a UV-vis detector. The chromatographic column that was used was a Phenomenex Kinetex C-18 (2.6 μm particle size; 4.6 × 150 mm). The mobile phase was 70% formic acid (0.1% v/v) and 30% acetonitrile (0.1% v/v) in isocratic mode and an elution flow rate of 0.35 mL min^{-1}. The injection volume was 100 μL in all samples. The detector wavelength was set at 264 nm for accurate identification of the antihistamine.

Determination of degradation by-products

The by-products of CP degradation were identified with a high efficiency liquid chromatograph (UPLC) (Waters, Acquity H Class model, USA) equipped with a C-18 analytical column (2.1 × 75 mm, 2.7 μm) (Waters) and coupled to a high-resolution mass spectrometer (Waters, model Xevo TQ-S, USA) equipped with a positive electrospray ionization system (UPLC/Q-TOF MS ESI); spectra were acquired in a mass range (m/z) between 50 and 1200 uma.

Cytotoxicity evaluation

The cytotoxicity evaluation of the degradation by-products was carried out through a cell viability assay (MTS) using two cell lines: human embryonic kidney (HEK-293) (85 120 602 (lot CB no. 2737)) and human liver (WRL-68) (89 121 403 (lot CB no. 2562)) cell lines from the CIC cell bank of the University of Granada. Prior to measurement, the degradation kinetics were studied in the presence of a biological buffer solution (PBS); then, 10 000 cells per well were seeded in a 96-well flat-bottom plate (Thermo-Fisher Scientific-Nunclon 96 flat) and incubated for 24 h, after which the medium was changed and the CP by-products were added. After another 24 h of incubation, 20 μL of MTS were added, and its absorbance was measured at 490 nm.

This journal is © The Royal Society of Chemistry 2020

Environ. Sci.: Water Res. Technol., 2020, **6**, 2607–2618 | **2609**

Results and discussion

OCX characterization

Morphological and textural characterization. Fig. 2(a) shows a scanning micrograph of the XBco material at 9070×. It can be observed that the sample has a compact surface as a result of the union of polymeric conglomerates. Morphological analysis revealed that the iron-incorporated materials (Fig. 2(b)) show a different structure from the reference material, with the presence of polymeric aggregates with particle sizes between 100 nm and 1 μm; this may be due to coalescence of the carbon microspheres during the sol–gel process.[26,27]

Elemental analysis *via* SEM revealed the presence of carbon and iron on the surface of the XFe-1.0 sample. Fig. 3 presents the micrograph of the elemental mapping, where Fe is highlighted in green. A polydisperse distribution of the metallic cation can be seen on the surface of the carbon nanoparticles.

The textural properties of the samples are presented in Table 2. The analysis revealed that the surface area as well as the volume and average pore diameter increased with the incorporation of the metallic ion in the gelation process. As can be observed, the XFe-1.0 ratio presented a greater surface area and pore volume, which can be attributed to the good distribution of the metal on the polymeric matrix; this ratio also indicates the development of microporosity,[27] in contrast to XBco, which presented the smallest surface area because of its densification. Meanwhile, the obtained isotherms are type IV according to IUPAC, which is a
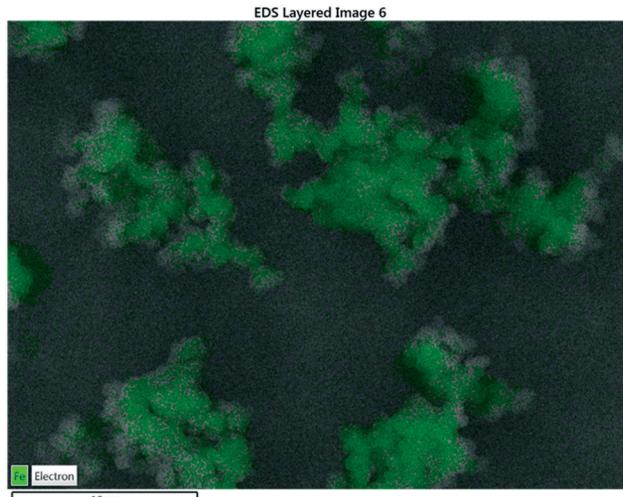

Fig. 3 EDS analysis of a sample of XFe-1.0.

characteristic of mesoporous materials. The XBco material showed a hysteresis loop of type H2, which can be assigned to pore blockage or percolation in a narrow range of pore necks; meanwhile, all the iron-incorporated materials presented a hysteresis loop of type H1, which is normally associated with porous materials consisting of agglomerates or compacts of uniform spheres.[19,28]

Surface physicochemical characterization. The functional groups on the surface of the OCX's were identified through Fourier transform infrared spectrophotometry (FTIR) and X-ray photoelectron spectroscopy (XPS). Fig. 4 shows the FTIR spectra of the XBco and XFe-1.0 samples; it can be observed that both show similar bands, and an O–H bond type stands out at 3300 cm^{-1}, which is characteristic of phenolic groups. There is also a stretching vibration around 2900 cm^{-1}, belonging to the C–H bond of aliphatic groups, which is represented at 1400 cm^{-1} as a deformation vibration; at 1710 and 1214 cm^{-1}, belonging to C=O and C–O bonds respectively, showing more intense bands in the XFe-1.0 because of the ligand insertion; at 1607 cm^{-1}, belonging to aldehyde or aromatic C=C bonds; and at 964 cm^{-1}, due to aromatic ring C–H bonds. It can be seen that the signal intensifies in the iron-incorporated material due to the presence of the metal complex.[21,29–31]

Using X-ray photoelectron spectroscopy, it was possible to obtain information about the molecular environment, oxidation state, and bonding atoms of the samples. Table 3 shows the elementary percentages of the representative samples, and Table 4 illustrates the atomic percentages of
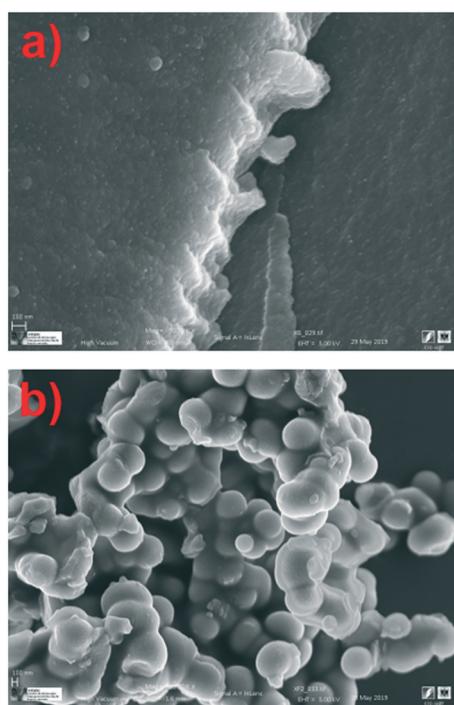
Fig. 2 Micrographs of samples of XBco (a) and XFe-1.0 (b) at 9070× and 3380×, respectively.

Table 2 Textural properties of the materials

Sample	S_{BET} (m^2 g^{-1})	V_p (cm^3 g^{-1})	D_p (nm)
XBco	1.08	0.0008	3.12
XFe-0.5	3.27	0.0046	5.63
XFe-1.0	11.47	0.0249	8.67
XFe-1.5	5.71	0.0083	5.84

2610 | *Environ. Sci.: Water Res. Technol.*, 2020, **6**, 2607–2618

This journal is © The Royal Society of Chemistry 2020
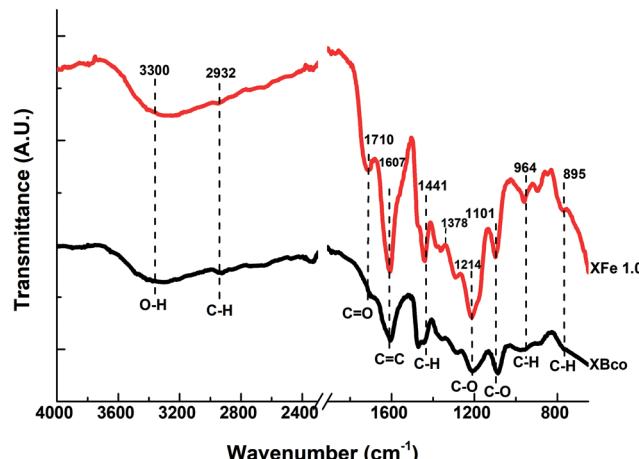
Fig. 4 FTIR spectra of samples of XBco and XFe 1.0.

Table 3 Elemental quantification of materials by XPS. The information is presented in atomic percentages

Sample	Fe2p	O1s	C1s
XBco	ND	23.59	76.41
XFe-0.5	0.42	33.36	66.22
XFe-1.0	0.89	30.93	68.18
XFe-1.5	0.42	36.32	63.26

the deconvolutions. Additionally, Fig. 5(a and b) presents the deconvolutions of C1s with the main peak at 285 eV, which can be deconvoluted into 3 peaks: the largest, at 284.6 eV, can be assigned to C–C bonds that are in the polymeric matrix of the carbonaceous material, while the peaks at 286.5 and 286 eV can be mainly attributed to C–O and C=O bonds belonging to the aromatic rings of resorcinol and to the single bonds of formaldehyde from the synthesis process, respectively.[29] Likewise, for O1s (Fig. 5(c and d)), three peaks can be deconvoluted: the first is at 531.2 and 531.4 eV for XBco and XFe-1.0, respectively, which correspond to the C=O bond, the second peak at 532 and 532.3 eV corresponds to the C–O bond, and the last peak appears at 534 eV, from which the correct bond of the polymeric structure can be verified by the C–O–C bond. Finally, for the deconvolution of the Fe2p region (Fig. 5(e)), a FeOOH bond was found at 711.5 eV, which confirms the chelation of the metal to the carbonaceous material through carboxylic groups belonging to the polymeric matrix. Meanwhile, the presence at 709 and

713 eV of Fe^{3+} oxides confirms the oxidation state of the element.[25]

Electrochemical characterization of the materials. Using diffuse reflectance UV-vis spectroscopy, the study of the electronic properties of the materials was carried out. Furthermore, as is already known, the photocatalytic activity of semiconductor materials is related to the band-gap energy (E_g);[33] calculation of E_g is possible from the diffuse reflectance spectra.

The Kubelka–Munk theory[34] allows us to analyze the diffuse reflectance from the diffuse component that provides information for the determination of E_g. This theory assumes that the incident radiation on a dispersing medium undergoes an absorption and dispersion process simultaneously. Assuming that the dispersion of the material is constant for the wavelength range in which it is being measured, it would only depend on the absorption coefficient, and the reflectance would be converted into the equivalent absorption coefficient, α, as shown in eqn (4):

$$F(R) = \frac{(1 - R_\infty)^2}{2R_\infty} = \alpha \qquad (4)$$

where $F(R)$ is the Kubelka–Munk function corresponding to the absorbance and R_∞ is the reflectance of a sample with infinite width with respect to a standard (barium sulfate) for each measured wavelength.

For different transition mechanisms, it has been shown that the energy of the incident photons and the energy of the band-gap (E_g) of the material in the absorption process can be determined by eqn (5):

$$(F(R) \times hv)^{\frac{1}{n}} = C(hv - E_g) \qquad (5)$$

where h is the Planck constant $(4.136 \times 10^{-15}$ eV s$^{-1})$, C is a fitting constant of the model, hv is the energy of the photon (eV), E_g is the band-gap energy (eV), and n is the constant that determines the type of optical transition, considering $n = 1/2$ for direct allowed transitions, as mentioned by other authors.[21] Furthermore, to minimize the adjustment error, a double linear fitting was performed, and the E_g value was obtained as the intersection point of both lines. Table 5 summarizes the E_g values and the respective activation energies of the materials (Fig. S1†) in the electromagnetic spectrum. It can be noted that when the metal was inserted into the polymeric matrix, E_g notably decreased; this is attributed to the fact that metal endows the material with

Table 4 Results of C1s, O1s and Fe2p deconvolutions using the XPS spectra of the samples (results are presented in atomic percentages)

Region	C_{1s}			O_{1s}			Fe_{2p}		
Peak	1	2	3	1	2	3	1	2	3
Bond	C–C	C–O	C=O	C=O	C–O	COOH	Fe_2O_3	FeOOH	Fe_2O_3
Energy, eV	284 ± 06	286 ± 0.5	288 ± 0.5	531 ± 0.5	532 ± 0.3	534 ± 0.3	709	711	713
XBco	38.63	44.10	17.25	4.33	65.40	0.43	—	—	—
XFe-1.0	39.61	38.59	21.92	17.19	82.37	30.26	5.05	34.76	60.17

This journal is © The Royal Society of Chemistry 2020

Environ. Sci.: Water Res. Technol., 2020, **6**, 2607–2618 | **2611**
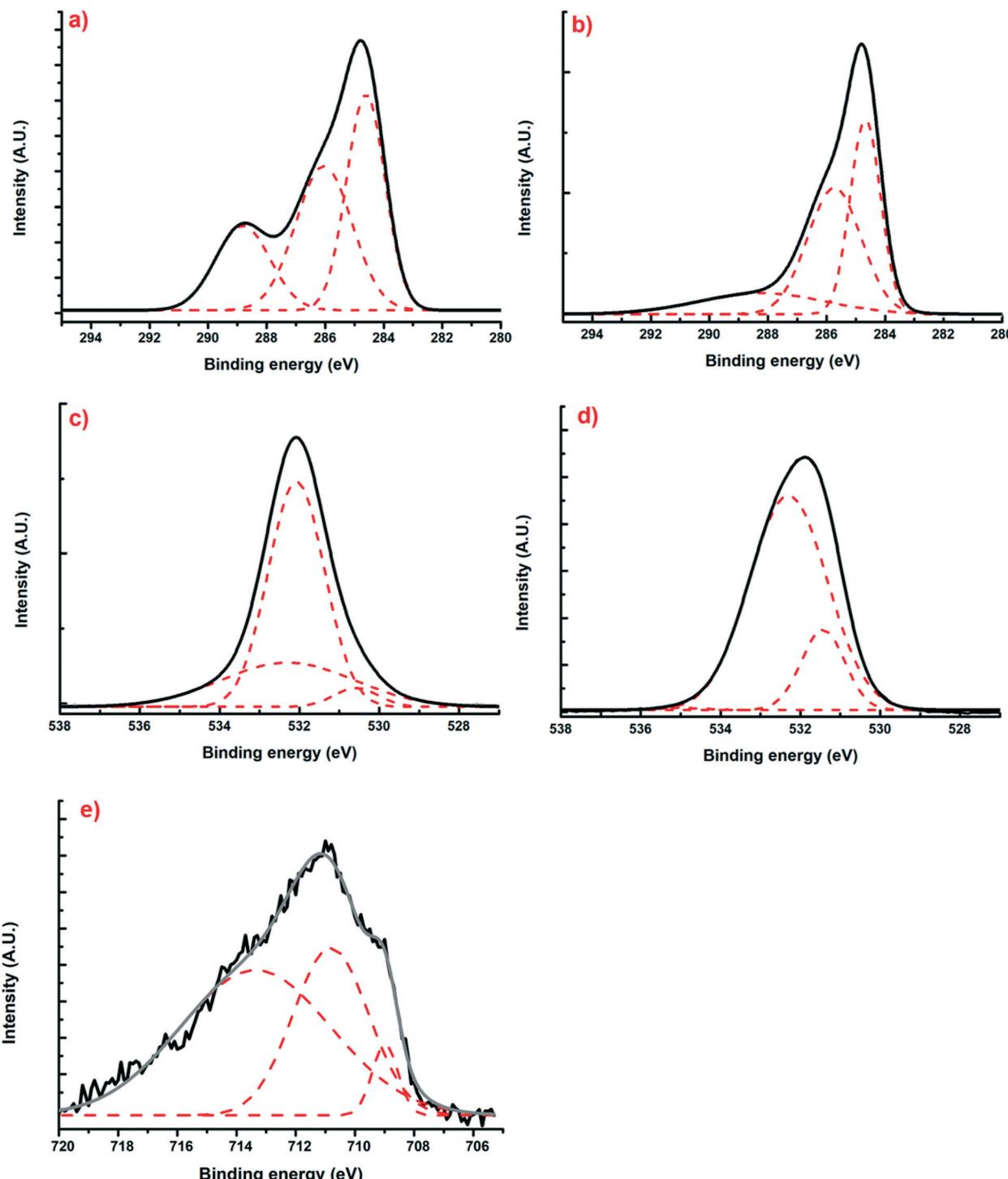
Fig. 5 Deconvoluted XPS spectra of regions C1s (a and b), O1s (c and d) and Fe2p (e) for samples of XBco and XFe-1.0, respectively.

Table 5 Band-gap values and activation energies according to the wavelengths determined for XBco and XFe at different molar ratios

Sample	Band-gap (eV)	Wavelength (nm)
XBco	5.5	225
XFe-0.5	1.8	688
XFe-1.0	2.2	564
XFe-1.5	2.1	590

better characteristics as a semiconductor material. In addition, it can be observed that the concentration of the metal in solution that was added during the synthesis process certainly influenced the activation energy of the material, which is more significantly recognizable in the activation spectrum of the material. The material that presented the highest E_g was the reference material; therefore, in order to activate the material, a higher intensity energy input is needed.

2612 | *Environ. Sci.: Water Res. Technol.*, 2020, **6**, 2607–2618

This journal is © The Royal Society of Chemistry 2020

Photoluminescence emission spectra help us to understand surface state changes, the efficiency of the charge-carrier capture, and electron–hole pair transfer and recombination.[35] The spectra of the samples were analyzed at a wavelength of 380 nm; different characteristic wavelength peaks appeared, demonstrating the presence of "trap sites" on the surface of the catalysts, as can be observed in Fig. 6.

These spectra corroborate that the iron-incorporated material presented a lower intensity in the recombination of the electron–hole pairs; therefore, the photo-oxidation process lasted longer. For the different metal ratios, no notable changes were observed in the presented intensities of the photoluminescence emission spectra.

Photochemical stability of the drug

Photolysis tests were performed on the CP drug to determine its stability in the presence of ultraviolet and solar irradiation at pH 3, C_{CP0} of 15 mg L^{-1} and room temperature. In Fig. 7, the degradation kinetics of the two types of irradiation can be compared, and it can be observed that the CP molecule has high stability to solar radiation. On the other hand, when using UV radiation, a considerable decrease in the initial concentration of the pollutant can be noted after 15 minutes. However, this technology entails a considerable cost; therefore, its large scale application is impractical.[36]

Indirect degradation of chlorpheniramine (CP)

The indirect degradation carried out for the various experiments is based on obtaining a better degradation response by implementing the use of a photocatalyst and radical-generating species, which together achieve better efficiency in this type of process. All the experiments were carried out indirectly with solar irradiation to check the efficacy of advanced oxidation processes in the degradation of the pollutant.

Degradation by the Fenton-like process. The degradation rate estimated with the first-order model[21] and the degradation percentage calculated with eqn (6) were


Fig. 7 CP degradation kinetics under different types of irradiation at pH 3.

considered as response variables in order to quantify the removal rate:

$$\%\text{Degradation} = \left(1 - \frac{C}{C_{CP0}}\right) \times 100\% \qquad (6)$$

where C is the concentration measured with respect to time and C_{CP0} is the initial concentration ($\sim$15 mg L^{-1}). Degradation percentages obtained are 15%, 14% and 16% in decreasing order of molar quantity of the iron-incorporated metal. It was observed that a smaller quantity of the metal favors the generation of $^\bullet$HO radicals for this process because it has a wider activation range in the electromagnetic spectrum in addition to a better distribution of the metal in the material. Table 6 shows the first order kinetic rate constants and degradation percentages.

Photodegradation by photocatalysis and heterogeneous photo-Fenton like processes. Various solar photodegradation tests were carried out with the materials. In this particular case, XFe 1.0 was the central material used for experimentation with the variables of catalyst dose, metal concentration, drug concentration, and addition of hydrogen peroxide. Moreover, hydrogen peroxide was added for the heterogeneous photo-Fenton like (HPFL) process. In Fig. 8, there was a noticeable decline in the initial concentration after 5 minutes in the HPFL process in comparison to the other processes; this can be corroborated in Table 7, which shows the degradation percentages of the drug and their respective kinetics fitted to a first order model. Likewise, XBco did not present any significant photocatalytic effects, as it needed a higher energy intensity to be activated.

Fig. 6 PL emission spectra of XBco and XFe-1.0.

Table 6 Fenton-like process operating conditions for the different metal ratios at pH 3 and 100 μL H$_2$O$_2$ for 60 minutes

Sample	$k \times 10^{-2}$ (min^{-1})	Degradation (%)
XFe 0.5	5.2	16
XFe 1.0	6.1	14
XFe 1.5	4.8	15

This journal is © The Royal Society of Chemistry 2020

Environ. Sci.: Water Res. Technol., 2020, **6**, 2607–2618 | **2613**
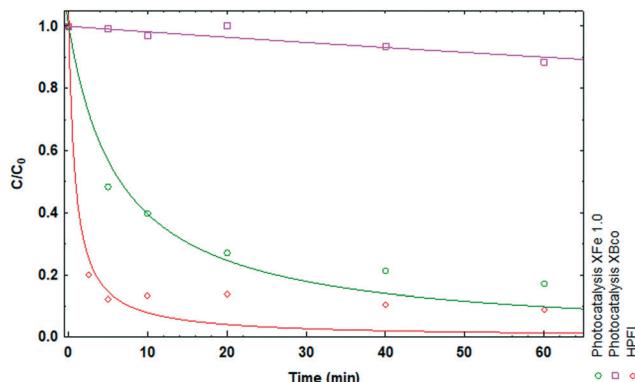
Fig. 8 Degradation kinetics of CP after 60 minutes using XBco and XFe 1.0 at pH 3.

Effects of the concentration of Fe impregnated in the OCX

The drug degradation was different according to the molar ratio of the chosen xerogel (0.5, 1.0 and 1.5). Considering that the xerogel with the least amount of metal degrades the best, Table 7 shows the degradation percentages in decreasing order as the concentration of the metal increases (93.4%, 82.9%, 71.0%). According to other authors, this can be attributed to obstruction of the pores of the material, which prevents the existing iron from interacting with the medium.[32]

Effects of the initial concentration of CP on its degradation with XFe

Different doses of the contaminant were tested to identify if the concentration of CP is a parameter that must be taken into account. The concentrations evaluated in the HPFL process were 7.5 mg L^{-1}, 15 mg L^{-1} and 30 mg L^{-1}. The results revealed that while the concentration of the drug is higher, it is necessary to form more $\cdot$HO radicals that can directly interact with the species and dissociate it. These results were corroborated by the kinetic data summarized in Table 7.

Effects of the catalyst mass on CP degradation

The mass of catalyst used partially influences the degradation percentage. The experiments carried out with the xerogels

XFe 0.5 and XFe 1.5 show degradation kinetics of 3.41×10^{-1} and 3.42×10^{-1} min^{-1}, respectively, when using 0.5 mg mL^{-1} of catalyst; when using 2.0 mg mL^{-1} of the catalyst, the kinetic constants are 3.02×10^{-1} and 4.1×10^{-1} min^{-1}. In general, the degradation percentages varied around 4%; thus, it can be stated that the concentration of the catalyst in the studied range is not significantly important in terms of the degradation rate, but it does affect the speed of the process. Due to possible supersaturation of radicals and catalyst, the contaminant cannot be adequately eliminated.

Determination of the $\cdot$HO radicals and e^-_{aq} in the solar photo-Fenton system

The elucidation of the action mechanism of OCX incorporated with Fe(III) was carried out using *tert*-butanol and NaNO$_3$ as inhibitors of the hydroxyl radical ($\cdot$HO) and the aqueous electron (e^-_{aq}), respectively. The results shown in Fig. 9 display that by inhibiting the $\cdot$HO radical, the degradation process is significantly slowed, while by blocking the e^-_{aq} pathway, the degradation process is not affected. Therefore, it can be assumed that the greatest contribution to the photodegradation of the drug is given by the hydroxyl radical.

Effects of synergy

Synergy is an important factor to take into account when analyzing various processes with a common purpose, such as the degradation of an antihistamine in this case; thus, the degradation percentages as well as their kinetic constants were calculated separately for the various experiments under similar conditions.

The contribution to the photocatalytic process was studied based on the response variable of the percentage degradation (eqn (7)). In the photocatalytic experiment, everything occurs together; for this reason, the other experiments are already in an implicit sum of the degradation percentage.

$$S_{Ptc} = \text{Photocatalysis} - \text{Photolysis} - \text{Adsorption} \qquad (7)$$

where S_{Ptc} is the photocatalytic synergy percentage of the various evaluated processes, adsorption, photolysis and

Table 7 Experimental conditions of CP degradation and evaluation of the different variables in the photocatalytic process and HPFL

Sample	C_{CP0} (mg L^{-1})	H_2O_2 (μL)	$k \times 10^{-1}$ (min^{-1})	Degradation (%)
XBco[b]	15	0	0.03	11.4
XFe 1.0[b]	15	0	0.92	82.9
XFe 1.0[b]	15	100	4.20	91.1
XFe 0.5[b]	15	0	1.29	93.4
XFe 1.5[b]	15	0	0.82	71.0
XFe 0.5[a]	30	50	3.01	66.0
XFe 0.5[a]	30	150	4.54	81.7
XFe 0.5[a]	7.5	50	3.41	87.2
XFe 1.5[a]	7.5	50	3.42	92.0
XFe 1.5[c]	30	150	4.1	86.3
XFe 0.5[c]	30	150	3.02	78.4

Weight/volume ratio: a = 0.5 mg mL^{-1}; b = 1 mg mL^{-1}; c = 2 mg mL^{-1}.
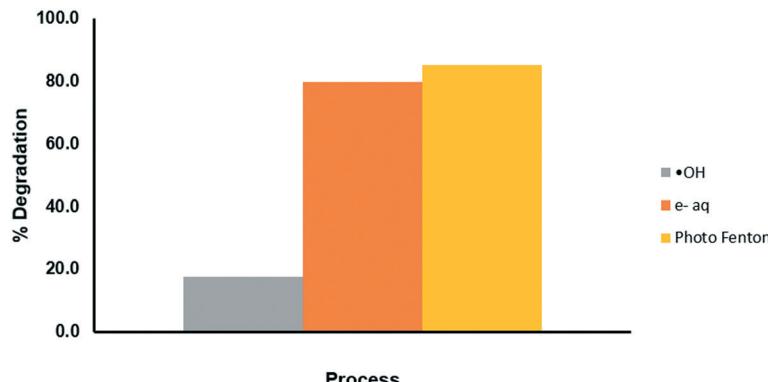
Fig. 9 Evaluation of the mechanisms of degradation of CP through the photo-Fenton process.

photocatalysis, while the synergy for the HPFL process was estimated using eqn (8):

$$S_{HPFL} = PhotoFenton - Fenton - S_{Ptc} \qquad (8)$$

Taking S_{HPFL} in the same way, the total synergy percentage of the various evaluated processes, namely HPFL, Fenton and photocatalysis (S_{Ptc}), was estimated with eqn (7).

The degradation percentages of the different processes are shown in Fig. 10. By applying the above equation, a 20% synergy of the HPFL process was obtained, which indicates that this process certainly contributes to the degradation of the drug.

Degradation mechanism

TOC analysis was performed for the HPFL process, for the photocatalytic process and for the pure material in irradiated aqueous medium. From the data obtained, it could be concluded that after 60 minutes, only 20% mineralization of the contaminant occurred because the material alone contributed to the TOC.

UPLC-MS analysis showed that in the various degradation processes that were studied, the by-products obtained had very similar molecular weights to the main product. Table 8 shows the addition of chlorine to compounds 2–6, which is

proposed to be due to the Cl^- in the buffer used to stabilize the pH of the solutions. This anion acts as an $^\cdot HO$ radical and e^-_{aq} scavenger, as indicated by Equations.[9–11] Additionally, a reduction in the number of carbons is observed mainly in compounds 4–6 and can also be attributed to the interaction of the chlorine anion or dichloro radical though their addition to the double bond or by electro-transfer reactions in the photocatalytic process and HPFL; this may be due to the generation of $^\cdot HO$, which interacts with the benzene rings and causes them to break down.[37]

$$Cl^- + {}^\cdot OH \rightarrow HClO^{\cdot-} \qquad (9)$$

$$HClO^{\cdot-} \rightarrow Cl^- + {}^\cdot OH \qquad (10)$$

$$HClO^{\cdot-} + e^-_{aq} \rightarrow Cl^- + HO^- \qquad (11)$$

Cytotoxicity of the degradation by-products

According to the tests carried out on the kidney cell line HEK-293 (Fig. 11a) and liver cell line WRL-68 (Fig. 11b), it was found that the by-products obtained from the various degradation systems had a cell viability greater than 75%; therefore, it can be considered that both cell lines have low toxicity levels. These cell lines were chosen by taking into
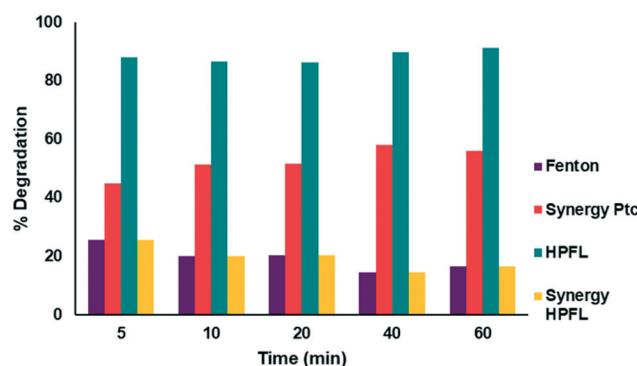
Fig. 10 Synergy of the photo-Fenton like process with respect to the other processes.

Table 8 By-products generated from the various degradation processes

	Process	Molecular formula	MW (g mol^{-1})	PPM	T_r (min)
1	Photolysis	$C_{16}H_{18}O_4$	274	1.8	3.44
2	Photolysis Photocatalysis HPFL	$C_{15}H_{24}Cl_2$	275	6.5	3.20
3	HPFL Photocatalysis	$C_{15}H_{24}OCl_2$	291	10.5	3.02
4	Photocatalysis HPFL	$C_{11}H_{19}N_4O_2Cl_2$	310	9.8	3.20
5	Photocatalysis HPFL	$C_{10}H_{24}N_2O_2Cl_2$	275	6.9	3.20
6	HPFL	$C_7H_{13}N_3Cl_2$	174.5	14.3	1.69

This journal is © The Royal Society of Chemistry 2020

*Environ. Sci.: Water Res. Technol.*, 2020, **6**, 2607–2618 | **2615**
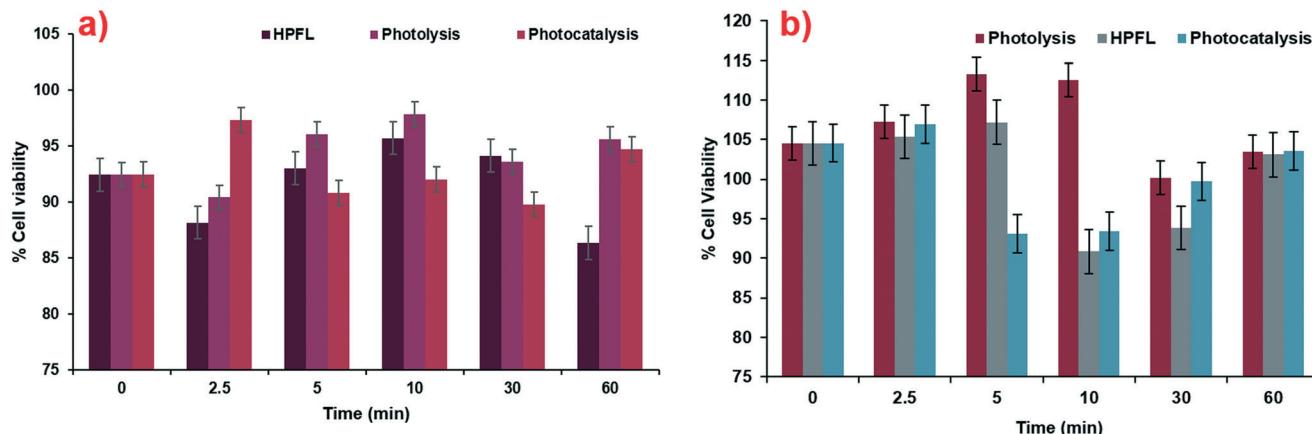
Fig. 11 Cytotoxicity of degradation by-products for various systems in a) HEK-293 cells and b) WRL-68 cells.
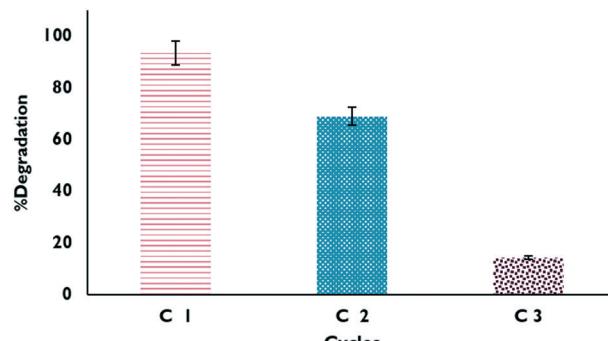
Fig. 12 Degradation percentages in the reuse cycles of XFe 1.0 in the HPFL process.

account the main negative effects that drugs have on these two organs.

Reuse cycles

The studied materials underwent a reuse process, where material that had been previously used was dried and reused for the degradation of the drug. The results obtained from the process are shown in Fig. 12; it can be verified that it is only possible to carry out a couple of reuse cycles of the material because after that, the effectiveness of the catalyst begins to decrease considerably. This may be due in part to Fe leaching or mass loss of the material during the experiments.

Conclusions

The results obtained from the various characterization techniques revealed the presence of Fe(III) attached to the polymeric matrix. Additionally, the introduction of this metal cation caused a significant decrease in the band-gap energy, enabling its activation in the visible region of the electromagnetic spectrum. The kinetic analysis indicated that the XFe 1.0 material had the highest degradation rate.

The heterogeneous photo-Fenton like process presented a 1.14 times higher degradation percentage than the photocatalytic process. This was attributed to the high rate of $^{\bullet}$HO radical formation, which was identified to be responsible for the degradation of the chlorpheniramine.

The by-products obtained from the various degradation systems correspond to compounds with molecular weights similar to the initial compound but with less complex structures; this confirms that chlorpheniramine is a molecule that can be degraded. Furthermore, cytotoxicity tests of the two cell lines corroborated the non-toxic nature of these by-products.

The experimental information collected reveals that the organic carbon xerogels with Fe(III) incorporated and used in heterogeneous photo-Fenton like processes are viable materials for application in oxidation treatments and disinfection of aqueous effluents by promoting the formation of high-power oxidant species.

List of abbreviations

HPFL	Heterogeneous photo-Fenton like
EC	Emerging contaminants
CP	Chlorpheniramine
WWTP	Wastewater treatment plants
AOP's	Advanced oxidation processes
MW	Molecular weight (g mol^{-1})
$^{\bullet}$HO	Hydroxyl radical
$O_2^{\bullet-}$	Superoxide radical
e^-_{aq}	Aqueous electron
H_2O_2	Hydrogen peroxide
OCX	Organic carbon xerogel
XBco	Organic carbon xerogel of reference
XFe	Organic carbon xerogel with iron
E_g	Band-gap (eV)
k	Rate constant (min^{-1})
C	Measured concentration of chlorpheniramine
C_{CP0}	Initial concentration of chlorpheniramine (mg L^{-1})
S_{PFC}	Synergy photocatalytic process

S_{HPFL} Synergy photo Fenton-like process

Conflicts of interest

There are no conflicts to declare.

Acknowledgements

References

1 Agua para todos, agua para la vida: informe de las Naciones Unidas sobre el desarrollo de los recursos hídricos en el mundo - UNESCO Biblioteca Digital [Internet], [cited 2020 Feb 26], Available from: https://unesdoc.unesco.org/ark:/48223/pf0000129556_spa.

2 C. Telegang Chekem, V. Goetz, Y. Richardson, G. Plantard and J. Blin, Modelling of adsorption/photodegradation phenomena on AC-TiO_2 composite catalysts for water treatment detoxification, *Catal. Today*, 2018, **328**, 183–188.

3 I. Quesada, U. Jáuregui, A. Wilhelm and H. Delmas, Contaminación de las aguas con productos farmacéuticos. Estrategias para enfrentar la problemática, *Rev. CENIC, Cienc. Biol.*, 2009, **40**(3), 173–180.

4 M. Williams, R. S. Kookana, A. Mehta, S. K. Yadav, B. L. Tailor and B. Maheshwari, Emerging contaminants in a river receiving untreated wastewater from an Indian urban centre, *Sci. Total Environ.*, 2019, **647**, 1256–1265.

5 BIO Intelligence Service and Executive Agency for Health and Consumers, *Study on the environmental risks of medicinal products*, 2013.

6 L. A. Kristofco and B. W. Brooks, Global scanning of antihistamines in the environment: Analysis of occurrence and hazards in aquatic systems, *Sci. Total Environ.*, 2017, **592**, 477–487.

7 S. N. F. Ali, E. I. El-Shafey, S. Al-Busafi, H. A. J. Al-Lawati, L. A. Kristofco and B. W. Brooks, *et al.*, An exposure assessment for selected pharmaceuticals within a watershed in Southern Ontario, *Chemosphere*, 2006, **64**(5), 717–729.

8 S. N. F. Ali, E. I. El-Shafey, S. Al-Busafi and H. A. J. Al-Lawati, Adsorption of chlorpheniramine and ibuprofen on surface functionalized activated carbons from deionized water and spiked hospital wastewater, *J. Environ. Chem. Eng.*, 2019, **7**(1), 102860.

9 M. H. Li, Acute toxicity of 30 pharmaceutically active compounds to freshwater planarians, Dugesia japonica, *Toxicol. Environ. Chem.*, 2013, **95**(7), 1157–1170.

10 E. E. Burns, J. Thomas-Oates, D. W. Kolpin, E. T. Furlong and A. B. A. Boxall, Are exposure predictions, used for the prioritization of pharmaceuticals in the environment, fit for purpose?, *Environ. Toxicol. Chem.*, 2017, **36**, 2823–2832.

11 M. T. Amin, A. A. Alazba and U. Manzoor, A review of removal of pollutants from water/wastewater using different types of nanomaterials, *Adv. Mater. Sci. Eng.*, 2014, 1–24.

12 R. A. Luna-Sánchez, B. B. Zermeño-Resendiz, E. Moctezuma, R. E. Contreras-Bermúdez, E. Leyva and M. A. López-Barragán, Fotodegradación de omeprazol en solución acuosa utilizando TiO_2 como catalizador, *Rev. Mex. Ing. Quim.*, 2013, **12**, 85–95.

13 E. Moctezuma, E. Leyva, M. López, A. Pinedo, B. Zermeño and B. Serrano, Photocatalytic degradation of metoprolol tartrate, *Top. Catal.*, 2013, **56**, 18–20.

14 M. Sánchez-Polo, J. Rivera-Utrilla, G. Prados-Joya and R. Ocampo-Pérez, Metronidazole photodegradation in aqueous solution by using photosensitizers and hydrogen peroxide, *J. Chem. Technol. Biotechnol.*, 2012, **87**(8), 1202–1208.

15 J. G. Mahy, L. Tasseroul, A. Zubiaur, J. Geens, M. Brisbois and M. Herlitschke, *et al.*, Highly dispersed iron xerogel catalysts for p-nitrophenol degradation by photo-Fenton effects, *Microporous Mesoporous Mater.*, 2014, **197**, 164–173.

16 S. Malato, P. Fernández-Ibáñez, M. I. Maldonado, J. Blanco and W. Gernjak, Decontamination and disinfection of water by solar photocatalysis: Recent overview and trends, *Catal. Today*, 2009, **147**, 1–59.

17 J. An, L. Zhu, N. Wang, Z. Song, Z. Yang and D. Du, *et al.*, Photo-Fenton like degradation of tetrabromobisphenol A with grapheneBiFeO_3 composite as a catalyst, *Chem. Eng. J.*, 2013, **219**, 225–237.

18 X. Zhang, J. Ma, C. Fan, M. Peng and S. Komarneni, Enhancement of photo-fenton-like degradation of orange II by MnO_2/NiO nanocomposite with the synergistic effect from bisulfite, *J. Alloys Compd.*, 2019, **785**, 343–349.

19 M. R. Carrasco-Díaz, E. Castillejos-López, A. Cerpa-Naranjo and M. L. Rojas-Cervantes, On the textural and crystalline properties of Fe-carbon xerogels. Application as Fenton-like catalysts in the oxidation of paracetamol by H_2O_2, *Microporous Mesoporous Mater.*, 2017, **237**, 282–293.

20 W. P. Kwan and B. M. Voelker, Rates of hydroxyl radical generation and organic compound oxidation in mineral-catalyzed fenton-like systems, *Environ. Sci. Technol.*, 2003, **37**(6), 1150–1158.

21 J. J. Salazar-Rábago, M. Sánchez-Polo, J. Rivera-Utrilla, R. Leyva-Ramos, R. Ocampo-Pérez and F. Carrasco-Marin, Organic xerogels doped with Tris (2,2′-bipyridine) ruthenium(II) as hydroxyl radical promoters: Synthesis, characterization, and photoactivity, *Chem. Eng. J.*, 2016, **306**, 289–297.

22 F. Orellana-García, M. A. Álvarez, M. V. López-Ramón, J. Rivera-Utrilla, M. Sánchez-Polo and M. Á. Fontecha-Cámara, Photoactivity of organic xerogels and aerogels in the photodegradation of herbicides from waters, *Appl. Catal., B*, 2016, **181**, 94–102.

23 C. J. Brinker and G. W. Scherer, *Sol-gel science: the physics and chemistry of sol-gel processing*, Academic Press, 1990, p. 908.

24 S. Álvarez, R. S. Ribeiro, H. T. Gomes, J. L. Sotelo and J. García, Synthesis of carbon xerogels and their application in

This journal is © The Royal Society of Chemistry 2020

Environ. Sci.: Water Res. Technol., 2020, **6**, 2607–2618 | 2617

adsorption studies of caffeine and diclofenac as emerging contaminants, *Chem. Eng. Res. Des.*, 2015, **95**, 229–238.

25 A. Acosta-Rangel, M. Sánchez-Polo, A. M. S. Polo, J. Rivera-Utrilla and M. S. Berber-Mendoza, Tinidazole degradation assisted by solar radiation and iron-doped silica xerogels, *Chem. Eng. J.*, 2018, **344**, 21–33.

26 Z. Liu, C. Lv and X. Tan, One-pot synthesis of Fe, Co and Ni-doped carbon xerogels and their magnetic properties, *J. Phys. Chem. Solids*, 2013, **74**(9), 1275–1280.

27 C. Moreno-Castilla, F. J. Maldonado-Hódar and A. F. Pérez-Cadenas, Physicochemical surface properties of Fe, Co, Ni, and Cu-doped monolithic organic aerogels, *Langmuir*, 2003, **19**(14), 5650–5655.

28 M. Ptaszkowska-Koniarz, J. Goscianska and R. Pietrzak, Synthesis of carbon xerogels modified with amine groups and copper for efficient adsorption of caffeine, *Chem. Eng. J.*, 2018, 13–21.

29 N. P. de Moraes, L. A. Bacetto, G. S. dos Santos, M. L. C. Pinto da Silva, J. P. B. Machado and T. M. B. Campos, *et al.*, Synthesis of novel ZnO/carbon xerogel composites: Effect of carbon content and calcination temperature on their structural and photocatalytic properties, *Ceram. Int.*, 2019, **45**(3), 3657–3667.

30 L. Tasseroul, S. L. Pirard, S. D. Lambert, C. A. Páez, D. Poelman and J. P. Pirard, *et al.*, Kinetic study of p-nitrophenol photodegradation with modified TiO$_2$ xerogels, *Chem. Eng. J.*, 2012, **191**, 441–450.

31 I. D. Alonso-Buenaposada, E. G. Calvo, M. A. Montes-Morán, J. Narciso, J. A. Menéndez and A. Arenillas, Desiccant capability of organic xerogels: Surface chemistry vs porous texture, *Microporous Mesoporous Mater.*, 2016, **232**, 70–76.

32 L. Shi, L. Yang, H. Zhang, K. Chang, G. Zhao and T. Kako, *et al.*, Implantation of Iron(III) in porphyrinic metal organic frameworks for highly improved photocatalytic performance, *Appl. Catal., B*, 2018, **224**, 60–68.

33 R. López and R. Gómez, Band-gap energy estimation from diffuse reflectance measurements on sol-gel and commercial TiO$_2$: A comparative study, *J. Sol-Gel Sci. Technol.*, 2012, **61**(1), 1–7.

34 N. P. de Moraes, M. L. C. P. da Silva and L. A. Rodrigues, Effect of metal doping in the photocatalytic properties of carbon xerogel-Nb$_2$O$_5$ composite towards visible light degradation of methylene blue, *Mater. Lett.*, 2018, **228**, 486–489.

35 S. Liu, X. Liu, Y. Chen and R. Jiang, A novel preparation of highly active iron-doped titania photocatalysts with a p-n junction semiconductor structure, *J. Alloys Compd.*, 2010, **506**(2), 877–882.

36 M. G. Peleyeju and O. A. Arotiba, Recent trend in visible-light photoelectrocatalytic systems for degradation of organic contaminants in water/wastewater, *Environ. Sci.: Water Res. Technol.*, 2018, **4**, 1389–1411.

37 L. Wang, J. Yang, Y. Li, J. Lv and J. Zou, Removal of chlorpheniramine in a nanoscale zero-valent iron induced heterogeneous Fenton system: Influencing factors and degradation intermediates, *Chem. Eng. J.*, 2016, **284**, 1058–1067.

2618 | *Environ. Sci.: Water Res. Technol.*, 2020, **6**, 2607–2618

This journal is © The Royal Society of Chemistry 2020